UNSTEADY COMPUTATIONS OF ROTOR-FUSELAGE INTERACTION

Mark Potsdam
Aerospace Engineer
US Army Aeroflightdynamics Directorate (AMRDEC), Moffett Field, CA, USA

Marilyn Smith
Associate Professor
Georgia Institute of Technology, Atlanta, GA, USA

Thomas Renaud
Research Engineer
Office National d'Etudes et de Recherches Aérospatiales, Meudon, France

ABSTRACT

Under the US-France Memorandum of Agreement on Helicopter Aeromechanics, ONERA, US Army, and Georgia Institute of Technology have performed full configuration, unsteady CFD analyses on a Dauphin helicopter configuration using individual, discrete moving blades. The three different multiblock, overset, and unstructured mesh calculations using compressible, unsteady low Mach preconditioning, and incompressible formulations are described. Spatial and temporal convergence studies are reported. Results are compared against ONERA wind tunnel data, including fuselage forces and unsteady surface pressures, rotor thrust, and wake PIV visualizations. Generally good agreement is seen between the partners' CFD calculations. At the flight conditions investigated, fuselage force comparisons with data are fair. Comparison of the PIV data with reasonably resolved CFD calculations shows clear qualitative agreement for wake strength and location. The CFD visualizations permit determining the origin of the flowfield structures in the PIV planes oriented streamwise and perpendicular to the mean flow. The flowfield and surface pressure visualizations indicate significant rotor-fuselage-empennage interactions which cannot be seen in lower-order actuator disk models.

1 NOMENCLATURE

C_DS	drag force, $\mathrm{Drag}/\frac{1}{2}\rho_\infty v_\infty^2$, m^2
C_LS	lift force, $\mathrm{Lift}/\frac{1}{2}\rho_\infty v_\infty^2$ m^2
C_SS	side force, $\mathrm{Side}/\frac{1}{2}\rho_\infty v_\infty^2$, m^2
c_p	pressure coefficient
C_T/σ	rotor thrust coefficient over solidity
(U)LMP	(unsteady) low Mach number preconditioning
R	rotor radius, 0.75 m
Re	Reynolds number, 1.07 million/m
S	rotor disk area, m^2
v_∞	freestream velocity, 15 m/s
v_{tip}	rotor tip velocity, ΩR, 100 m/s
X_b	rotor-fuselage axial force, 0
Z_b	rotor-fuselage thrust (200 C_T/σ), 14.5
α	pitch angle, -3 deg
β	steady LMP parameter, typically $3M_\infty^2$
β_{1s}	rotor lateral flapping, 0 deg
μ	advance ratio, v_∞/v_{tip} = 0.15
ρ_∞	freestream fluid density, kg/m^3
σ	rotor solidity, 0.0849
ψ	rotor azimuth angle, 0 deg aft, + clockwise

2 INTRODUCTION

The application of Computational Fluid Dynamics (CFD) for rotorcraft analysis and design offers great promise, but continued research is required into the efficiency, accuracy and capability of the methodologies to capture the unsteady, complex flow physics around realistic fuselage configurations. This is an important research topic since fuselage drag can account for up to one-third of total helicopter drag. In addition, rotor-fuselage interactions are complex and may have a major influence on both the helicopter fuselage, especially the empennage, and rotor flowfields.

Under the US-France Memorandum of Agreement (MOA) on Helicopter Aeromechanics, the US Army Aeroflightdynamics Directorate (AFDD), the Georgia Institute of Technology (GIT), and the French Office National d'Etudes et de Recherches Aerospatiales (ONERA) have been involved in a task to investigate rotor-fuselage interaction. As part of this effort, a comparative study of the Dauphin 365N helicopter has been undertaken to analyze the capabilities and weaknesses of state-of-the-art CFD codes.

While rotor-fuselage interactions can be efficiently computed with a momentum source actuator disk modeling the rotor, the results are time averaged, leading to a quasi-steady representation of the flowfield. Previous work by the authors investigated the isolated fuselage and fuselage with varying degrees of actuator disk fidelity.[1] Time-averaged wake features were well captured using a non-uniform actuator disk when compared with 5-hole probe experimental measurements. Fuselage force and moment results were only in fair agreement with data. Grid convergence studies were performed. Fuselage surface pressures were well predicted except in the separated region behind the engine pylon/doghouse. Results were insensitive to turbulence modeling. With current supercomputing power and overset grid strategies, the rotor-fuselage interaction for a complete helicopter with individual moving blades can now be simulated by an unsteady viscous computation.

Full rotor-fuselage helicopter configuration CFD calculations are now fairly common in research environments, but are still considered state-of-the-art due to being manpower (i.e. grid generation) and computationally intensive. Recent unsteady rotor-fuselage interaction (RFI) work includes compressible calculations on the Dauphin,[2] overset grid calculations on the CH-47 Chinook,[3] simulations on the NASA ROtor-Body INteraction (ROBIN) model,[4,5,6] and numerous calculations on the European GOAHEAD configurations.[7,8,9]

This paper further investigates the rotor-fuselage interaction on the Dauphin configuration using unsteady, discrete, moving rotor blades. The Dauphin model and experimental test campaigns are described in Section 3. Section 4 describes the CFD methodologies and computational grids used by the partners, including numerical parameters. The results section (Section 5) discusses the need for some form of unsteady low Mach number preconditioning and investigates grid density effects, numerical accuracy, and grid and unsteady solution convergence. Comparisons are made between the partners' results and with experimental test data (fuselage forces/moments, fuselage steady and unsteady surface pressures, and PIV wake visualization). Finally, conclusions are drawn (Section 6).

3 DAUPHIN CONFIGURATION

At ONERA, a Dauphin helicopter model (Figure 1) equipped with a powered main rotor was designed and tested in the S2Ch wind tunnel in the late 1980's. Several new test campaigns have recently been carried out in the F1 subsonic wind tunnel (4.5 m x 3.5 m) and provide more detailed experimental results along with error analysis,[10] including steady and unsteady fuselage surface pressures, balance measurements, and 2D and 3D PIV wake measurements.

The tested helicopter model is a 1/7.7 Dauphin model equipped with a powered main rotor. The length of the fuselage is equal to 1.5 m. The 0.75 m radius 4-bladed rotor is articulated in pitch, flap and lead-lag motions. The 0.05 m constant chord blade uses OA209 airfoils and has -12 deg/R of linear twist. The blade root cutout is at 0.275R. The clockwise rotor rotation is ensured by an electric engine which allows a blade tip speed of 100 m/s (1272 RPM).

A fuselage devoted to steady pressure measurements is equipped with 234 steady pressure transducers, while a separate fuselage devoted to unsteady pressure measurements includes 44 transducers. In the S2Ch measurements, two balances measure the aerodynamic forces and moments for each part of the model: one balance measures the global forces on the fuselage and the rotor; the other one measures only the rotor. The subsequent and more detailed F1 tests provide more reliable pressure measurements for the test case investigated in this paper, but only a single combined 6-component rotor and fuselage balance measurement.

The experimental fuselage model varies somewhat from the theoretical Dauphin 365N model definition, especially in the area of the engine inlet and exhaust fairings. The model also has no fenestron tail rotor, which is faired over. A digitized geometry has been obtained by ONERA and developed into CFD grids at AFDD. Computational comparisons between the experimental and theoretical geometries by GIT and AFDD show only minor effects on fuselage forces and moments. Therefore, the theoretical geometry has been used for all the current calculations. A facsimile of the rotor hub is included in the AFDD and GIT calculations. The model strut has been excluded. In order to prevent binding of the balance, a small gap exists between the strut and the fuselage bottom surface. For pressure comparisons, these holes have been sealed in the F1 experiments so that the experimental geometry correlates more closely with the computational one, which does not model these gaps. The wind tunnel walls were not modeled. A CFD run by GIT showed that there was minimal impact on the isolated fuselage results, indicating only minor blockage effects.

4 COMPUTATIONAL MODELING

In this work, the full configuration Dauphin rotor and fuselage has been analyzed with different CFD codes by the three partners. Initially each code used a different gridding strategy: multiblock, overset and unstructured,[1] however, in order to handle the geometric complexity of the discrete, moving rotor blades and allow for wake capturing, all partners have resorted, at least in part, to an overset grid capability.

All the CFD codes solve the unsteady Reynolds-averaged Navier-Stokes (URANS) equations. When flight conditions are within the incompressible regime and a compressible formulation is used, the relative insensitivity of the density, compared to the other primitive variables such as pressure and velocity, and the large difference between the acoustic and convective speeds cause the compressible equations to become ill-conditioned, resulting in poor convergence and accuracy. Low Mach number preconditioning is a method whereby the system of equations are locally modified by a preconditioning matrix which equalizes the eigenvalues and rescales the artificial dissipation, thus improving both convergence and accuracy of the steady or unsteady compressible flow equations. In addition, one of the solvers applied in the research can solve the incompressible form of the RANS equations via the artificial compressibility method of Chorin.[11]

Due to the constraints of the individual numerical methods, the partners each used their own grid around the Dauphin 365N geometry. Approximately 7 million points on the fuselage was respected. The first grid point off the surface (1.1×10^{-5} m) results in calculated y^+ values typically less than 1.

4.1 OVERFLOW 2.0

4.1.1 Numerical Algorithm

AFDD calculations use the Reynolds-averaged Navier-Stokes computational fluid dynamics code OVERFLOW 2.0.[12,13,14] It offers numerous spatial and temporal algorithm options, turbulence models, and boundary conditions. In the Chimera domain decomposition methodology,[15] geometrically complex configurations are reduced to a set of relatively simple overlapping grids. Solutions are computed on node-centered, structured, overset grids made up of body-conforming curvilinear “near-body” grids and automatically-generated Cartesian “off-body” grids.[12]

For the calculations on the Dauphin, OVERFLOW 2.0 runs use 2nd-order spatial central differencing in the near-body grids and 4th-order in the off-body grids. For stability this is combined with 4th-difference matrix artificial dissipation (DIS4 = 0.02), resulting in a scheme that is formally 3rd-order accurate. No 2nd-order artificial dissipation is required. A 2nd-order implicit diagonalized approximate factorization temporal scheme with dual-time stepping is used. Within the pseudo-time subiterations, a constant CFL number (based on local velocity), typically 12 to 24, is used. A baseline time step equivalent to 0.25° (1440 steps per revolution) is used along with 20 dual-time stepping subiterations, generally resulting in a two order subiteration residual drop. Because of the low advance ratio, approximately 3 rotor revolutions are performed in order to obtain a periodic solution. To speed convergence, the unsteady calculation is initiated from a steady fuselage result.

The Spalart-Allmaras turbulence model[16] is used in the near-body grids, which are assumed fully turbulent. A thin-layer approximation is used, and viscous terms are activated only in the wall normal direction. Off-body grids are modeled as inviscid in order to reduce the numerical dissipation in the wake.

Unsteady, moving body problems are handled using subroutine-activated hole cutting (object x-rays) and domain connectivity. The domain connectivity and flow solver modules have been parallelized for efficient, scalable computations on large parallel computers using the Message Passing Interface (MPI) protocol. However, load balancing is based on node count partitioning for the flow solver, which is not optimal for hole cutting. Because of the significant amount of flow solver work required per time step with the dual-time stepping subiterative scheme, the overall domain connectivity expense is minimal and up to 95% parallel efficiency is obtained.

Unsteady solutions on the finest grid (40.0 M points) were computed on 192 processors of an IBM Power6, requiring 11.6 hours per rotor revolution. The equivalent serial processing rate is 139 μsec/node/time step.

4.1.2 Blended ULMP

An unsteady low Mach number preconditioning (ULMP) scheme is used for accurate and efficient computations with the flow conditions and geometry investigated here (M_∞ = 0.044). Motivated by this problem, the baseline ULMP dual-time stepping scheme in

OVERFLOW[17] was modified for improved accuracy and convergence.[18] The artificial dissipation was re-formulated as a "blended" dissipation scheme that uses the steady preconditioning scaling for the velocity and temperature fields and the unsteady preconditioning scaling for the pressure field. The scheme has the advantage of reverting back to the standard steady preconditioning formulation for steady flows and, compared with previous implementations, removes most of the dissipation dependence on physical time step. Moreover, the blended formulation allowed a straightforward extension to matrix artificial dissipation. The stability, convergence, and accuracy of the blended scheme were verified using von Neumann stability analysis and computations of a simple vortex propagation problem.[18]

The scheme requires user input of both steady and unsteady preconditioning parameters. In the current analyses, the steady low Mach number preconditioning parameter, β, which controls accuracy on the right-hand side (RHS) of the discrete equations, is set to the standard value, $3M_\infty^2$. The unsteady parameter, β_u, which controls convergence on the left-hand side (LHS), is set to 1.0 for the current calculations ($\sqrt{\beta_u} = L_{ref}/c\pi\Delta t$). β_u of 1.0 corresponds to no preconditioning and is entirely warranted due to the relatively small time step size used.

4.1.3 Grid Generation

AFDD uses overset structured meshes, with near-body grids generated with the NASA-developed, overset grid generation software OVERGRID. The viscous near-body fuselage grids extend out a distance of 10% of the fuselage length. The 30 overlapping fuselage near-body grids contain 4.9 million grid points. Automatically-generated Cartesian off-body grids extend to the far field (Figure 2b). C-grid topology meshes are generated for the blade grids along with overlapping root and tip cap grids (Figure 3b). The main blade meshes are dimensioned 249x49x49, with 189 points on the airfoil and a total of 1.48 million points per blade. They extend away from the surface approximately 1.2 chords with an initial spacing at the wall of 3.0×10^{-6} m, resulting in y^+ less than 1.5 at all blade positions. The entire rotor-fuselage configuration is embedded in a nested Cartesian grid system. The finest grids which surround the fuselage and blades have a spacing of 20% of the blade chord (0.01 m). The resulting grid system contains 98 overlapping meshes and 14.9 million points. A coarser mesh with 2.1 million grid points and 40% chord wake spacing was used to evaluate convergence characteristics of the numerical schemes. A fine mesh with reduced wake spacing of 10% chord and the baseline near-body grids was used for wake visualizations. It contains 40.0 million grid points.

4.2 elsA

4.2.1 Numerical Algorithm

ONERA has utilized for this effort the object-oriented code elsA[19,20] (Ensemble Logiciel de Simulation en Aérodynamique). The Reynolds-averaged Navier-Stokes equations are solved via a finite volume formulation. Multiblock structured meshes permit the efficient modeling of a wide variety of complex configurations (fixed-wing aircraft, turbomachinery, helicopter, etc.). The 2nd-order spatial discretization of the conservative system is ensured by the space-centered Jameson scheme. The 2nd and 4th-order coefficients of the Jameson artificial viscosity are equal to 0.5 and 0.016, respectively. For the Navier-Stokes computations, the k-ω turbulence model is used with the SST correction and the Zheng limiter. The calculations do not include any transition criteria.

The time integration is done with a backward Euler scheme and an LU scalar relaxation implicit phase. A sub-iterative 2nd-order Newton-like Gear method allows convergence acceleration with the use of large azimuthal time steps. The computations have been performed for at least 3 rotor revolutions in order to get satisfying convergence of the solutions. The chosen physical timestep corresponds to 1° per iteration. For each timestep, 40 Gear sub-iterations are used in order to have a global residual decrease of at least 2 orders. The Navier-Stokes calculations require about 140 hours CPU time for one rotor revolution on a NEC SX6 single processor.

Due to a lack of robustness on the fine mesh, low Mach number preconditioning has not been used in the ONERA computations.

4.2.2 Grid Generation

A Chimera method[21] simplifies the process of mesh generation by using overlapping grids. ONERA generated a point-matched, multiblock grid with the ICEM-CFD software, where an actuator disk surface is directly meshed (Figure 2a). This fine grid has a total of about 7.4 million points distributed in 97 blocks. This

grid represents the background grids onto which the blades meshes are overlapped. The blade grid (Figure 3a) contains 181x57x41 points (~1.7 million points for the 4 blades). About 120 points are distributed on each airfoil surface and 30 sections in the spanwise direction.

4.3 FUN3D

4.3.1 Numerical Algorithm

Georgia Tech has employed the NASA-developed FUN3D code.[22,23,24] FUN3D solves the RANS equations using an implicit solver on unstructured mixed element or fully tetrahedral meshes. The user has the option of resolving either the compressible or incompressible flow regimes using a backward Euler time discretization. Incompressible flows are resolved using the Chorin[11] artificial compressibility method. An option also exists whereby the compressible equations of motion can be applied to low Mach number flows via an unsteady low Mach number preconditioning method[25] modified partially using the method developed by Potsdam[18] and described previously. The resulting linear system of equations is solved using a point-implicit relaxation scheme. The Spalart-Allmaras turbulence model is selected for these simulations. The flow variables are stored at the vertices of the unstructured cells and solved on the non-overlapping dual control volumes that surround each node using a node-based algorithm. Roe's flux difference splitting technique[26] is applied to the inviscid fluxes on the control volume faces, while an equivalent central difference approximation is achieved for the viscous flux computations via a finite volume formulation.

The solutions for this work were computed with the unsteady, incompressible option. The solution was advanced with a time step equivalent to 1°. During each timestep, 15 sub-iterations are used to ensure 1-2 orders of magnitude residual reduction during each time step. Ten turbulence sub-iterations were also applied to converge the loosely-coupled turbulence model.

The computations were performed on 64 2.3GHz processors of a CRAY XT5. The mean required CPU time is 781 μsec/node/timestep, which includes the sub-iteration costs. Runs typically require 3-4 rotor revolutions for force and moment convergence with prescribed rotor blade motion.

4.3.2 Grid Generation

NASA's VGRIDns[27] was used to generate a fully tetrahedral, overset mesh for unstructured FUN3D computations. The overset strategy allows mesh refinement near the fuselage and rotor blades (Figure 2c), while minimizing the number of overset meshes. Each rotor blade (Figure 3c) is enclosed in a rectangular near-body boundary that extends 2 chords (2c) normal to the surface, (-2.5c, 3.5c) forward and aft of the blade, and 4c beyond the tips. A coarse mesh consisting of 0.63 million nodes (3.7 million cells) and a refined mesh of 1.2 million nodes (7.1 million cells) comprised each near-body blade grid. The background grid, which included the fuselage, consisted of 1.2 million nodes (7.2 million cells) for the coarse grid and 8.8 million nodes (51.6 million cells) for the refined grid. The outer boundary of the fuselage grid is set to 4 fuselage lengths, based on prior experience[4] with rotor-fuselage interaction problems using FUN3D.

5 RESULTS

In the F1 experiments, the Dauphin configuration is trimmed to a specified thrust (Z_b = 14.5), axial force (X_b = 0), and rotor lateral flapping (β_{1s} = 0). The baseline flow conditions used exclusively for this work are v_∞ = 15 m/s (M_∞ = 0.044, μ = 0.15), -3° fuselage angle of attack (nose down), and zero sideslip. These conditions result in wake impingement on both the fuselage and empennage and are, therefore, appropriate for investigation of rotor-fuselage interaction. The Reynolds number is 1.07 million/meter. The rotor shaft angle is -4° relative to the fuselage. For the computational results, rotor control angles (collective, flap, lag and their first harmonics, including cyclic) are obtained from the rotorcraft comprehensive code HOST,[28] rather than from direct experimental measurements, which were not deemed sufficiently accurate due to variation of 0.5 to 1.0 deg between test campaigns. Therefore, fuselage interference effects have not been included in the rotor trim. The rotor blades are reasonably modeled as rigid and no CFD/CSD coupling is performed with the comprehensive analysis to iterate on trim, although all the CFD codes have these capabilities.

5.1 Numerical Effects of Compressibility

The impact of compressibility and unsteady low Mach number preconditioning (ULMP) on the time-accurate, unsteady flow field has been investigated by AFDD on the coarse grid.

Regarding accuracy, Figure 4a shows the effect of preconditioning on the *steady* fuselage drag, as a function of the preconditioning parameter, β[1]. Variation of up to a factor of 3 is seen, with drag typically decreasing as more preconditioning is applied. Large oscillations in the time-averaged upper centerline surface pressures and unreasonable stagnation pressures for the unsteady calculation are seen in Figure 4b when comparing unpreconditioned results with steady LMP (used in an unsteady calculation). The time-averaged fuselage forces also differ between the unpreconditioned and preconditioned solutions as shown in Table 1.

Table 1 – Effect of preconditioning on fuselage forces, coarse grid (AFDD)

Precond	subiter	C_LS	C_DS	C_SS
No	20	-0.047	0.018	-0.020
Steady	400	-0.029	0.012	-0.016
Blended	20	-0.030	0.012	-0.018

Regarding convergence, the blended ULMP method provides convergence improvements in relation to steady LMP. Figure 5 shows that for the same level of subiteration residual convergence in pseudo-time, steady preconditioning (b) may require up to six times more work than no (a) or blended (c) preconditioning, in addition to being less stable. The situation is actually even worse than it appears. The same level of subiteration convergence with steady preconditioning does not result in a converged solution, as shown in the fuselage lift histories (Figure 6), so that the overall disadvantage can be up to a factor of 20 for a fully converged solution. Although the no preconditioning forces appear well converged in Figure 6a, the poor accuracy, as noted by the different scale in this figure, must be considered. Figure 4b also shows that the blended dissipation scheme used in ULMP has little effect on the surface pressures compared with steady preconditioning. It is seen then that blended ULMP offers significantly improved accuracy compared with no preconditioning and faster convergence compared with steady preconditioning. For further details the reader is referred to Reference 18.

Surface pressure contours using an incompressible formulation in FUN3D are compared in Figure 7 with compressible results to demonstrate the impact of the different RANS formulations on the surface pressures. The compressible surface pressures indicate that the solution is rapidly changing (oscillating) from grid cell to cell rather than smoothly varying as expected. The incompressible formulation, however, appears smooth and does not exhibit the oscillatory behavior across grid cells. This phenomenon is particularly noticeable on the forward fuselage deck and engine housing/hub.

5.2 Numerical Convergence

5.2.1 Spatial Convergence

All partners investigated the effects of mesh refinement on their solutions. Due to space constraints, a limited sampling of the results is shown for the fuselage forces, rotor forces, and wake.

Mesh refinement for the isolated, steady fuselage has been performed previously.[1] For example, a fine fuselage grid is seen to improve the results with a smoother solution, and fuselage drag compares better with the experiment. For the unsteady analysis ONERA results indicate improved lift and drag prediction with mesh refinement (Figure 8) and with test data, in spite of the lack of ULMP. In this mesh refinement analysis, only the fuselage grid has been changed, however, Figure 9 shows that the refinement also affects the rotor solution, indicating the importance of the rotor-fuselage coupling and interactions. Indeed, the rotor thrust is decreased with the finer fuselage mesh by about 2%, and enrichment of the harmonic content of the rotor thrust evolution is seen.

Grid convergence of the wake is shown in AFDD calculations in Figure 10. As the grid spacing in the uniform Cartesian wake mesh is decreased, improved capturing of the super-vortices, individual root and tip vortices, rotor blade wake sheets, and empennage wake is obtained. It should be noted that individual tip vortices are still on the order of the finest wake spacing used (10% chord). Figure 11 shows the effect of mesh refinement on blade airloads at the 97% span location. The blade-wake interactions and higher frequency content are increasingly captured with the finer rotor and wake mesh. Unlike the ONERA results presented in Figure 8, AFDD saw less effect on integrated fuselage forces with wake grid refinement. There was also minimal effect on fuselage and rotor forces as a function of the dissipation scheme used in the wake (scalar and matrix with and without blended preconditioning).

GIT ran two different grids, which were relatively comparable to the coarse and baseline AFDD structured grid systems. The

coarser GIT grid results in very large oscillations in the fuselage integrated forces, which are much larger than those observed by the other partners, although the time-averaged values correlate well. ONERA and AFDD also observed a reduction in the oscillations for the integrated fuselage force histories during grid refinement. The oscillatory behavior observed in the GIT integrated fuselage force history is also observed in the solution residual history. The refined grid and the coarse grid show relatively comparable residual levels for each variable, however, there are large variations about the mean residual values for the coarse grid that disappear when the refined grid is utilized (Figure 12).

The coarse grid oscillations also resulted in a significant drag (0.035), which dropped (0.024) when the grid was refined, similar to the grid refinement observations by ONERA (Figure 8). Since AFDD does not encounter similar phenomena during its grid refinement, it may be attributable to their ULMP methodology. This implies that a similar undertaking to increase the accuracy of the drag could be explored for the FUN3D unsteady incompressible method to improve the performance of the code for less refined grids. Finally, it should be noted that the GIT background grid refinement was similar to the 0.4c and 0.2c wake grid refinement study carried out by AFDD (Figure 10), and the flow field feature refinement observed was similar.

In all cases, wake spacings on the order of 40% chord are insufficient to provide reasonable wake capturing. This level of cell size is more appropriate for isolated fuselage or actuator disk calculations[1]. All partners observed that finer grids actually reduced the high frequency content of the fuselage force histories.

5.2.2 Temporal Convergence

ONERA performed temporal convergence studies by varying time step and number of subiterations using the Gear time integration on the coarse grid. Figure 13 presents the time convergence history of the rotor thrust, and Figure 14 shows the time convergence history of the fuselage lift. The effects of the number of subiterations, azimuthal time step, and total number of iterations (constant value of subiterations/$\Delta\psi$ = 40 subiter/°) are plotted. A reference solution (black curves) is chosen with ($\Delta\Psi$, subiter) = (1°, 80). It is obvious that increasing the number of subiterations or decreasing the physical time step improves the solution convergence, but it is important to find a compromise in order to avoid a CPU cost which is too high. The 1° solutions require more than 20 subiterations for convergence, where 40 sub-iterations correspond to a mean global residual reduction of 3 orders. In the second set of analyses, the solution with ($\Delta\Psi$, subiter) = (0.5°, 20) compares well with the reference solution, whereas a time step of 2° does not capture the phase and the amplitude of the aerodynamic phenomena. The third set of graphs confirms this conclusion; even if the number of sub-iterations is increased up to 80. The parameters ($\Delta\Psi$, subiter) = (0.5°, 20), (1°, 40) and (1°, 80) provide very similar results. However, as shown in Table 2, the CPU cost per rotor revolution (obtained on a NEC SX6 processor) is higher for the smallest physical time step. This is essentially due to the overset research (data exchange and hole cutting) which is performed at each time step but not during subiterations. Therefore, the best compromise for this configuration seems to be the solution given by a 1° azimuthal time step and 40 subiterations.

Table 2 – CPU cost comparison for temporal convergence study (ONERA)

$\Delta\psi$ (deg)	Subiterations	CPU time per rotor revolution (sec)
1	80	320
0.5	20	310
1	40	229
2	80	152

AFDD investigated temporal convergence using no, steady, and blended preconditioning, as described in section 5.1. With steady preconditioning, fuselage force history convergence is obtained only after 400 subiterations, although convergence of rotor force histories and integrated, time-averaged quantities can be achieved much sooner. Without preconditioning, robust convergence can be obtained, but accuracy is poor. Temporal convergence characteristics as a function of time step were also investigated. Baseline values of 0.25° and 20 subiterations are finally chosen as a good compromise between accuracy and efficiency. A minimum 2 orders of magnitude reduction in the subiteration residual is usually obtained.

Further temporal convergence studies were performed using steady preconditioning. Overall it was found that integrated and time-averaged quantities were insensitive to time step and subiteration count for time steps as large as 1.0°. Fuselage force histories were

most sensitive to temporal convergence, compared with the rotor and wake. Constant work solutions (subiter/$\Delta\psi$ = constant iteration/degree) gave similar results as long as the solutions were at least relatively converged. However, larger time steps may miss important flow phenomenon while only slightly reducing (<10%) the computational cost due to reduced domain connectivity (hole cutting) overhead (Note: this is contrary to elsA conclusions regarding Chimera efficiency).

GIT did not perform extensive temporal grid studies for this analysis, but used the results of similar studies[4,29], which showed that the 1^{o} time step with 15 sub-iterations was sufficient for the simulations. A verification check was made for the coarse grid using 30 sub-iterations and the results showed that the same behavior resulted with less than 0.5% change in the integrated fuselage loads and rotor thrust.

5.3 Fuselage Forces/Moments

Comparison of the fuselage forces and moments are shown in Table 3 against S2Ch data. In spite of the lack of preconditioning and, therefore, perhaps fortuitously, the ONERA results for lift and drag are in reasonable agreement. On the other hand, the AFDD and GIT lift results appear to be in much closer agreement with each other, although further from the S2Ch experiment. Conversely the AFDD and GIT drag results are above and below the experimental drag value by the same (large) increment, while ONERA's drag result appears most accurate. For AFDD the underprediction of drag may be partly attributable to the S-A turbulence model implementation.[1] GIT's side force result is approximately one-half the value of the AFDD and ONERA results, and is in relatively good agreement with experimental value. Preliminary ONERA results using preconditioning in only the fuselage grid blocks are more similar to the other partners' computational results.

Figure 15 compares the fuselage lift and drag force histories from the three partners, which corroborate the averaged fuselage forces from Table 3. In addition, it is observed that the character of the forces over time is comparable, in particular for lift. The 4/rev frequency content in the AFDD drag is clearly observed, while the GIT and ONERA drag histories contain more prominent higher frequency content. As discussed previously, this may be an artifact of the AFDD ULMP algorithm.

Table 3 – Fuselage forces

	C_LS	C_DS	C_SS
S2Ch	-0.0401	0.0178	-0.0055
ONERA	-0.0392	0.0159	-0.0174
AFDD	-0.0293	0.0112	-0.0149
GIT	-0.0313	0.0243	-0.0066

5.4 Fuselage Pressures

Steady fuselage pressures on the upper surface centerline are shown in Figure 16. They have been averaged over one rotor period (90 deg). The different codes are in good agreement with each other and the experimental data, except in the region aft of the pylon. Numerous investigations into this area (grid refinement, geometric fidelity, higher-order turbulence modeling) have failed to provide a clear understanding of the dependency of the separation on numerical effects. The GIT simulations have been able to correctly capture larger portions of the flow characteristics with grid refinement and adaptation, but this was not repeatable by AFDD. This implies that there is a very complex interdependency of the turbulence modeling implementation with the overall numerical algorithm and grid structure that is distinct in each methodology. Therefore, in spite of the extra computational effort for the unsteady calculations, these results remain in similar agreement with those obtained using an actuator disk model.[1] However, only the unsteady simulations are able to show realistic unsteady fuselage effects and rotor-fuselage interactions due to discrete blade tip vortices, as described in this section and section 5.6 on wake visualization.

The rotor unsteadiness has a significant effect on the fuselage flow field. The time history and magnitude/frequency content of the pressure coefficient at two locations on the fuselage upper centerline compare well to the experimental pressure transducer data in Figure 17. The strong 4-per-rev content due to the 4-bladed rotor is accurately captured by all the results. Higher frequencies, especially 4N-per-rev, are also seen. The magnitude of the rotor-fuselage interaction is stronger on the tail boom (transducer 27) than the fuselage nose (transducer 4), as indicated in both the data and the calculations. GIT results appear slightly out of phase and of reduced magnitude compared with the other simulations.

Figure 18 shows a sequence of surface pressure differential contours as a function of blade azimuth. The mean fuselage pressures have been removed. The global influence of the discrete blades (wake downwash and pressure impulse) on the fuselage upper and

side surfaces is seen as each blade approaches the fuselage centerline and then passes over it (recall clockwise rotor rotation). Detailed pressure changes on the empennage from 10-20 degree azimuth indicate a discrete vortex passage, which induces significant unsteadiness on both the horizontal stabilizer and left vertical fin.

The overall unsteady behavior is similar for AFDD and GIT, but a difference can be observed between the 14° and 18° azimuth locations. The strong discrete wake passage observed by AFDD has significantly less impact in the GIT results, indicating that the wake downwash and/or vortical strength is much less and with different phasing. At 60 degrees azimuth, the wake interaction with the vertical tail is observed in both simulations at approximately the same location.

5.5 Rotor Loading

Predictions of the rotor thrust based on the HOST control inputs are shown in Table 4. There is good agreement between AFDD and ONERA results although the CFD results underpredict the measured thrust by 7%. The GIT results are significantly lower with 18% underprediction. The underpredictions are attributable to assumptions made in HOST and could be remedied with CFD/CSD coupling. The differences in rotor trim may affect locations of the wake structures compared with experimental data.

Figure 19 compares the rotor thrust time histories from the three partners along with the HOST result. Some higher harmonics are seen. Also shown is the section normal force at the 97% span station. At the low advance ratio flight conditions investigated here, there are two significant blade-wake interactions around 90° and 270° azimuth. These are best captured with fine mesh spacings (Figure 11).

Table 4 – Rotor thrust

	Z_b
F1	14.5
HOST	14.765
ONERA	13.36
AFDD	13.50
GIT	11.76

5.6 Wake Visualization

A range of F1 PIV wind tunnel measurements were performed in 10 planes around the configuration, parallel and perpendicular to the freestream.[10] Images were synchronized at 32 rotor azimuth locations (every 11.25°) and are the result of averaging 120 instantaneous images taken over approximately 2 minutes. Because of inherent unsteadiness, blade-to-blade differences and trim imbalance, and vortex wandering, it is expected that an ensemble average of PIV images would tend to smear out the wake features (vortices and shear layers) and reduce the peak magnitudes. The errors in velocity and vorticity have been estimated at 3% and 10%, respectively.[10] Smooth variation of the measurements across different PIV planes reflects the good repeatability.

General views of the CFD wakes using the Q-criterion are shown in Figure 20 for the three different solvers. The Q-criterion is well known to be able to highlight vortical structures while deemphasizing shear layers compared with vorticity-based visualization. AFDD results use the finest wake grid, which has better resolution than the other two solvers, in addition to the use of the higher-order numerical scheme.

The visualizations are clearly able to pick up the blade tip and root vortices. For the AFDD visualization these vortices are significantly increased in size once they enter the off-body grids. The tip vortices dissipate after traveling a distance of approximately one rotor radius, but this dissipation distance is subjectively based on the chosen value of the Q iso-surface. Levels that visualize more of the downstream wake tend to obscure other salient features. The velocity deficit in the wake of the vertical tail is seen upon interaction with the tip vortices. Tip vortices emanating from the fins and vertical tail are apparent. The super-vortices are seen along with the realistic roll-up of the discrete tip vortices around these large structures in the AFDD simulation. The blade root vortices also roll up and coalesce on the left side of the fuselage and impact the left horizontal tail at this advance ratio. This effect may be somewhat overestimated due to a lack of blade root shank modeling and the large root cutouts.

Comparisons of the CFD calculations with the time-dependent PIV data are shown in Figure 21 and Figure 22 in planes behind the empennage and on the advancing and retreating sides of the rotor, respectively. In all the figures, one of the rotor blades is at 0° azimuth. The experimental and CFD contours use the same vorticity scales. All CFD simulations identify the primary features, but the impact of the wake refinement accomplished by AFDD is most clearly prominent. Thus, the details of the wake discussion comparing CFD with experiment

will be with respect to the AFDD results, except where noted.

In the plane perpendicular to the freestream (Figure 21), located 1.0125 m (1.35R) behind the rotor center, a number of flow features are identified in both the experiment and simulations. In general there is excellent agreement between CFD and PIV in the strength and location of the flow structures, especially on the advancing (left) side. On the retreating (right) side all the CFD features appear to be shifted further inboard and downward relative to the PIV structures. As such, it is unclear if the two blue vortex structures on the retreating side at the edge of the middle image in the PIV can correspond to the ones in the CFD image which emanate from the vertical fin. This would indicate a large amount of outward flow (opposite the swirl velocities) compared with the CFD calculation. It is possible that this mismatch may be partly attributable to the offset in rotor thrust or variations in rotor trim.

Since the CFD calculations contain the full wake (i.e. Figure 20) it is straightforward to trace the vorticity origins in order to clarify the features seen in the two-dimensional PIV planes, where the vorticity sources are not at all obvious. This allows for differentiation between discrete root and tip vortices, wake sheets, empennage vortices, and fuselage interactions. The origin of the vortical structures in Figure 21 can be explained with reference to the AFDD numerical labels.

In both the CFD and PIV data, the super-vortices (1) are asymmetric, with the advancing (A) side being higher than the retreating side (R). The details of the tip vortices rolling up around the super-vortices are seen, also with noticeable asymmetry.

Tip vortices 2A and 2R were shed two blade passages previously in the aft quadrants (quadrants 1 and 4) and directly connect with each other. They are the youngest vortices seen as they are the highest up and have not been ingested into the super vortices. Tip vortex 3A was also shed in quadrant 1 and is 90° older than 2A. 3R has already passed completely through the plane. Tip vortices 4AR, 5AR and 6AR were shed in the forward quadrants (2 and 3). They are significantly older, 6-8 blade passages previous, having traveled a longer distance to reach the PIV plane. 4AR are in the process of being ingested into the super-vortices and are, therefore, stretched and less distinct. Different CFD snapshots indicate that the oldest (6AR) tend to wander.

The right vertical fin lower vortex (7) has the same sign as super-vortex 1A and indicates that the fin is generating a side force to the left to counteract the rotor torque. Note that the right upper vertical fin vortex cannot be seen, while the left is ingested in the large blade root/empennage interaction (10). The vertical tail emits a wake sheet and vortex 8, which indicates that it is also lifting left. Vortex 9 emanates from the right horizontal/vertical fin junction.

From Figure 20 it is seen that all the blade root vortices tend to bundle together on the left side of the pylon. From there they are convected downstream to interact with the left horizontal tail and vertical fin (10). It is also seen in Figure 21 that some of the older tip vortices from the front of the rotor disk, having been disrupted and stretched by passing through the fuselage, are rolling up around this structure.

The advancing (11-15) and retreating wake sheets indicate that the downwash is much stronger on the advancing side. On the advancing side, 5 wake sheets indicate 5 blade passages, however, only the first 4 are visible in the PIV image. The advancing wake sheets in the AFDD calculation appear as somewhat discrete, individually-spaced vortices. Although they are perhaps reminiscent of Taylor-Görtler vortices, in this case they are a numerical artifice, probably related to the overset interpolation between the well-defined viscous wake off the blade C-mesh and the poor interpolation into the coarser Cartesian background grid. These artifices have been seen in the past to be a function of the background spacing. They are not seen when blade O-meshes are used due to more consistent overlap[3], albeit with no wake sheet capturing ability.

Counter-rotating vortex pairs 16 and 17 roll off the fenestron and fuselage lower surfaces, respectively.

Given the complicated nature of the flow in this plane, which is in close proximity to the empennage, it is easy to see the difficulty that the rotorcraft designer faces in avoiding adverse rotor-empennage interactions across a range of flight conditions. It gives one additional insight as to why so many rotorcraft empennages (e.g. RAH-66, AH-64) have faced redesign in flight test. These results indicate that unsteady velocity-based CFD calculations have reached a level of accuracy and maturity that they can now be used to investigate these interactions much earlier in the design cycle.

Figure 22 shows a comparison of y-vorticity on 2D PIV planes on the retreating side of the rotor. The agreement is not as satisfying as for the empennage plane, although many of the main features are present in both.

Using the AFDD results for detailed comparisons with PIV, it is clear that the strongest tip vortices are matched reasonably well. Vortex 1A is only ~35° old, emanating from the blade currently at 0° azimuth and having been initiated at 325° azimuth, the aft (A) part of the rotor disk. Tip vortices 2-4F are 3-5 blade passages old, having emanated from the front (F) of the rotor disk and with opposite y-vorticity sign. Some of the wake sheets are also in agreement. Overall, however, the AFDD CFD results tend to be more discrete than the experimental results. This could be due to poor wake sheet capturing due to a lack of sufficient grid resolution. Issues related to intergrid interpolation described above may apply.

The GIT results show a higher wake and, along with ONERA, a more diffuse wake than in the PIV and AFDD results. For GIT this is indicative of the observed lower thrust and higher drag. Vortex wander in the PIV could also account for smearing of the vortices, particularly for the trail from the forward part of the disk, which one might expect to be more discrete based on the tip vortices seen in CFD visualizations.

6 CONCLUSIONS

Calculations using three CFD solvers by partners in the US-France MOA on Helicopter Aeromechanics (AFDD, ONERA, GIT) have been performed on an unsteady, rotor-fuselage interaction configuration. The Dauphin helicopter configuration was run at a low freestream Mach number (M_∞ = 0.044). The simulations used a range of compressible, incompressible, and unsteady low Mach preconditioning formulations of the turbulent Reynolds-averaged Navier-Stokes equations on structured and unstructured, overset grids. Fuselage and rotor loads, time histories, and surface pressures along with wake visualizations are compared between simulations and with ONERA F1 wind tunnel data, including PIV. The following conclusions are drawn:

- For the low Mach freestream conditions investigated, it is necessary to employ an incompressible or preconditioned compressible numerical formulation in order to obtain accurate and smooth results. For the time steps considered (0.25 – 1.0 deg azimuth), temporal convergence must be monitored for an efficient solution.
- The incompressible solver convergence and accuracy improves with grid resolution. Further algorithm development may be warranted to improve simulations using coarser grids.
- Spatial convergence studies indicate that wake mesh spacings which may be appropriate for isolated fuselage or actuator disk calculations are not generally sufficient for unsteady, moving body calculations, especially when detailed wake geometries and interactions are sought. Background grid wake spacings of at most 10% blade chord reduce numerical dissipation and allow for more detailed wake capturing. Less resolved wakes (up to 20% chord) can provide reasonable fuselage forces and pressures while still capturing basic wake features. A clear potential for higher-order schemes with adaptive mesh refinement (AMR) is seen.
- CFD simulations with resolved wakes show excellent qualitative comparison with experimental PIV data. In addition, the sources of vorticity seen in PIV planar data can much more easily be explained and elucidated by reference to the complete 3D wake geometry from CFD. CFD results coupled with a CSD solver to permit trimming to the wind tunnel conditions may improve the wake feature correlations.
- The three overset grid methods, structured and unstructured, provide overall comparable correlation with the experimental data as well as generally good agreement between the partners CFD results on equivalent grids. Agreement with wind tunnel data for steady and unsteady surface pressures and rotor loads is good, while fuselage force agreement with data is inconsistent.
- Prediction of fuselage pressures in the separated region aft of the engine fairing/pylon was problematic. The empennage surface pressure in areas of complex geometry and flow separation are an intricate interaction of the grid and flow solver, and guidelines are not readily extracted from a parametric study.

7 ACKNOWLEDGEMENTS

The authors would like to thank Arnaud Le Pape, the F1 wind tunnel test team, and the PIV group (from the Applied Aerodynamics Department) at ONERA for providing the experimental data. The authors are grateful to Eurocopter for the Dauphin 365N geometry. The GIT authors would like to acknowledge the support provided by the National Rotorcraft Technology Center (NRTC) at the Georgia Institute of Technology. Dr. Mike Rutkowski is the technical monitor. Computational support for AFDD and GIT was provided through the

High Performance Computing and Modernization Program DoD Supercomputer Resource Center (DSRC) at NAVO. These resources are gratefully acknowledged. The GIT allocation is through an HPC grant from the US Army (S/AAA Dr. Roger Strawn). Prof. Smith would like to thank Mr. Rajiv Shenoy and Mr. Phillip Richards at Georgia Tech for their help during the study.

8 REFERENCES

1 Renaud, T., O'Brien, D., Smith, M., and Potsdam, M., "Evaluation of Isolated Fuselage and Rotor-Fuselage Interaction Using CFD," *Journal of the American Helicopter Society*, Vol. 53, No. 1, January 2008, pp. 3-17.

2 Renaud, T., Le Pape, A., and Benoît, C., "Unsteady Euler and Navier-Stokes Computations of a Complete Helicopter," 31st European Rotorcraft Forum, Florence, Italy, September 2005.

3 Bhagwat, M., Dimanlig, A., Saberi, H., Meadowcroft, E., Panda, B., and Strawn, R., "CFD/CSD Coupled Trim Solution for the Dual-Rotor CH-47 Helicopter Including Fuselage Modeling," AHS Specialists' Conference on Aeromechanics, San Francisco, CA January 2008.

4 O'Brien, D. M., Jr., "Analysis of Computational Modeling Techniques for Rotorcraft Configurations," PhD Dissertation, Georgia Institute of Technology, Atlanta, GA, April 2006.

5 Kenyon, A., and Brown, R., "Wake Dynamics and Rotor-Fuselage Aerodynamic Interactions," Journal of the American Helicopter Society, Vol. 54, No. 1, 012003, January 2009.

6 Nam, H., Park, Y., and Kwon, O., "Simulation of Unsteady Rotor-Fuselage Aerodynamic Interaction Using Unstructured Adaptive Meshes," *Journal of the American Helicopter Society*, Vol. 51, No. 2, pp 141-148, April 2006.

7 Pahlke, K., "The GOAHEAD Project," 33rd European Rotorcraft Forum, Kazan, Russia, September 2007.

8 Boelens, O., van der Ven, H., Kok, J., and Prananta, B., "Rotorcraft Simulations Using a Sliding Grid Approach," 34st European Rotorcraft Forum, Liverpool, England, September 2008.

9 Stiejl, R., and Barakos, G., "Computational Analysis of Rotor-Fuselage Interactional Aerodynamics Using Sliding-Plane CFD Method," 34st European Rotorcraft Forum, Liverpool, England, September 2008.

10 Le Pape, A., Gatard, J., and Monnier, J.-C., "Experimental Investigations of Rotor-Fuselage Aerodynamic Interactions," *Journal of the American Helicopter Society*, Vol. 52, No. 2, April 2007, pp. 99-109.

11 Chorin, A. J., "A Numerical Method for Solving Incompressible Viscous Flow Problems," *Journal of Computational Physics*, Vol. 2, No. 1, 1967, pp. 12-26.

12 Chan, W., Meakin, R., and Potsdam, M., "CHSSI Software for Geometrically Complex Unsteady Aerodynamic Applications," AIAA Paper 2001-0593, AIAA 39th Aerospace Sciences Meeting and Exhibit, Reno, NV, January 2001.

13 Buning, P. G., Gomez, R. J., and Scallion, W. I., "CFD Approaches for Simulation of Wing-Body Stage Separation," AIAA 2004-4838, 22nd AIAA Applied Aerodynamics Conference, Providence, RI, August 2004.

14 Jespersen, D., Pulliam, T., and Buning, P., "Recent Enhancements to OVERFLOW," AIAA Paper 1997-644, AIAA 35th Aerospace Sciences Meeting and Exhibit, Reno, NV, January 1997.

15 Steger, J., Dougherty, C., and Benek, J., "A Chimera Grid Scheme," Advances in Grid Generation, K. N. Ghia and U. Ghia, eds., ASME DEF-Vol. 5, June 1983.

16 Spalart, P. and Allmaras, S., "One-equation turbulence model for aerodynamic flows," AIAA Paper 92-0439, 1992.

17 Pandya, S., Venkateswaran, S., and Pulliam, T., "Implementation of Preconditioned Dual-Time Procedures in OVERFLOW," 41st AIAA Aerospace Sciences Meeting and Exhibit, Reno, NV, January 2003, AIAA 2003-0072.

18 Potsdam, M., Sankaran, V., and Pandya, S., "Unsteady Low Mach Preconditioning with Application to Rotorcraft Flows," AIAA Paper 2007-4473, 18th AIAA CFD Conference, Miami, FL, June 2007.

19 Gazaix M., Jollès A., Lazareff M., "The *elsA* Object-Oriented Computational Tool for Industrial Application", 23rd ICAS Conference, September 2002.

20 Cambier L., Veuillot J. P., "Status of the elsA CFD software for flow simulation and multidisciplinary applications", 48th AIAA Aerospace Science Meeting and Exhibit, Reno, NV, January 7-10, 2008.

21 Benoît, C., Le Pape, M.-C., Jeanfaivre, G., "Improvement of the Robustness of the Chimera Method," 32nd AIAA Fluid Dynamics Conference & Exhibit, St. Louis, MO, June 2002.

22 Anderson, W., and Bonhaus, D., "An Implicit Upwind Algorithm for Computing Turbulent Flows on Unstructured Grids," *Computers & Fluids*, Vol. 23, No. 1, 1994, pp. 1-21.

23 Anderson, W., Rausch, R., and Bonhaus, D., "Implicit/Multigrid Algorithms for Incompressible Turbulent Flows on Unstructured Grids," *Journal of Computational Physics*, No. 128, 1996, pp. 391-408.

24 Bonhaus, D., *An Upwind Multigrid Method for Solving Viscous Flows on Unstructured Triangular Meshes*, M.S. Thesis, George Washington University, 1993.

25 Abras, J. N., "Enhancement of Aeroelastic Rotor Airload Prediction Methods," PhD Dissertation, Georgia Institute of Technology, Atlanta, GA, March 2009.

26 Roe, P., "Approximate Riemann Solvers, Parameter Vectors and Difference Schemes," *Journal of Computational Physics*, No. 43, 1981, pp. 357-372.

27 Pirzadeh, S., "Three-Dimensional Unstructured Viscous Grids by the Advancing Layers Method," *AIAA Journal*, Vol. 34, (1), January 1996, pp. 43-49.

28 Benoît, B., Dequin, A.-M., Kampa, K., Grunhagen, W., Basset, P.-M., and Gimonet, B., "HOST, A General Helicopter Simulation, Tool for Germany and France," 56th Annual Forum of the American Helicopter Society, Virginia Beach, VA, May 2002.

29 Shenoy, R., Smith, M., Kenyon, A., and Brown, R., "Vorticity-Transport and Unstructured RANS Investigation of Rotor-Fuselage Interactions," *Proceedings of the 35th ERF Forum*, Hamburg, Germany, September, 2009.

Figure 1 – Dauphin 365N fuselage in ONERA F1 wind tunnel

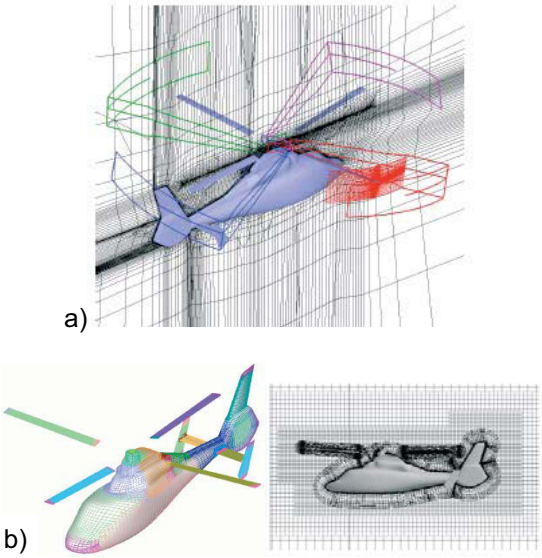

Figure 2 – CFD fuselage grids, a) ONERA, b) AFDD, c) GIT

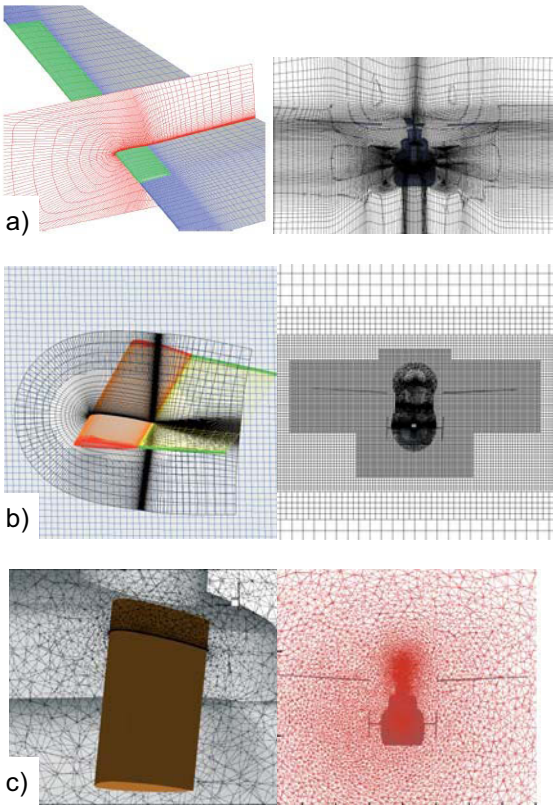

Figure 3 – CFD rotor blade and wake grids, a) ONERA, b) AFDD, c) GIT

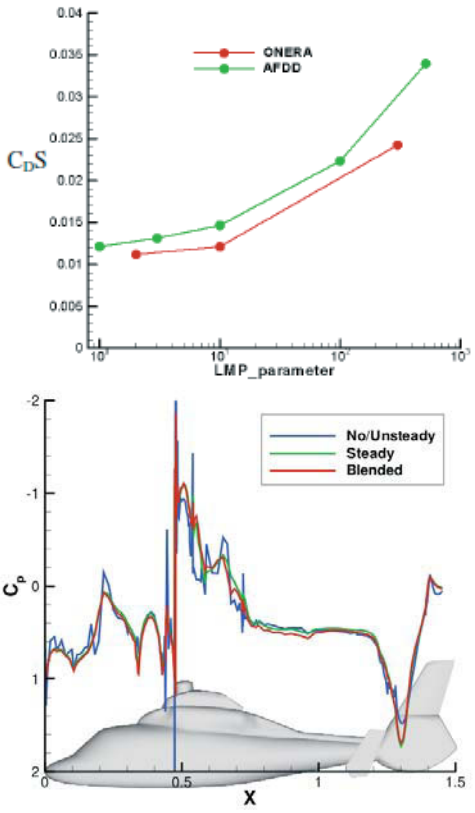

Figure 4 – Effect of LMP on a) steady integrated drag force and b) unsteady time-averaged upper centerline surface pressures (AFDD)

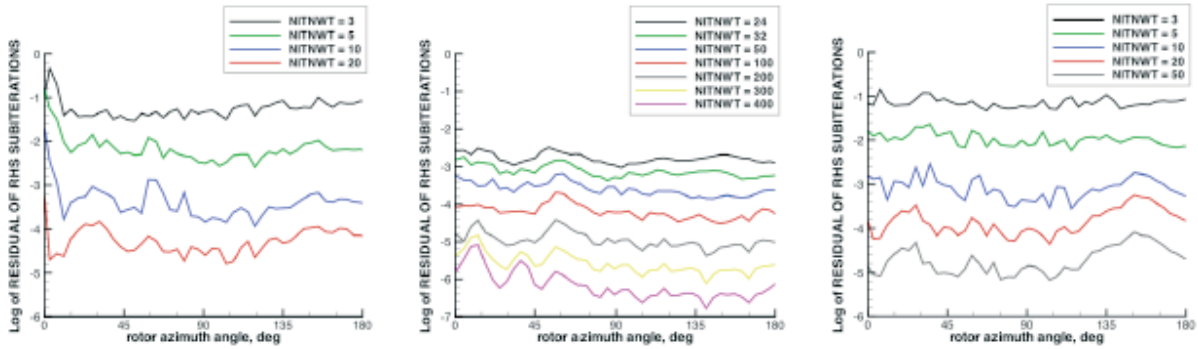

Figure 5 – Subiteration convergence as a function of preconditioning formulation and number of subiterations (NITNWT) – a) no preconditioning, b) steady, c) blended preconditioning, coarse grid (AFDD)

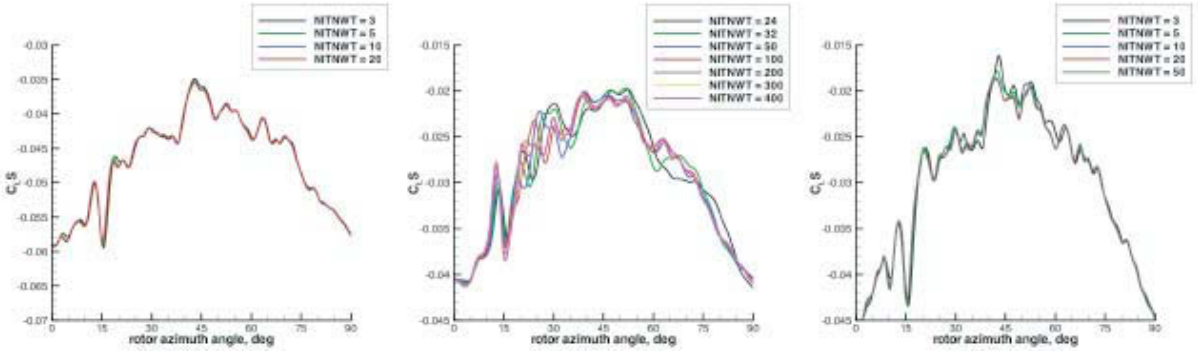

Figure 6 – Fuselage lift history convergence as a function of preconditioning formulation and number of subiterations (NITNWT) – a) no preconditioning, b) steady, c) blended preconditioning, coarse grid (AFDD)

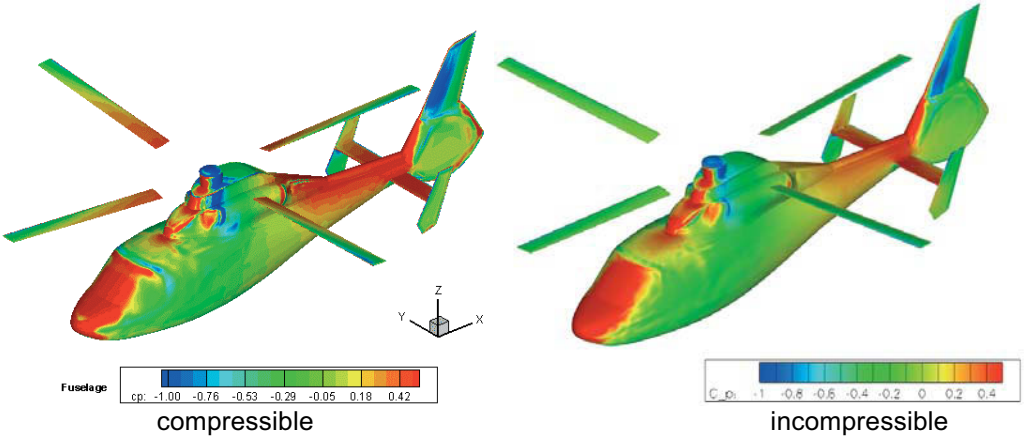

Figure 7 – Effect of compressible/incompressible formulation on fuselage surface pressures (FUN3D)

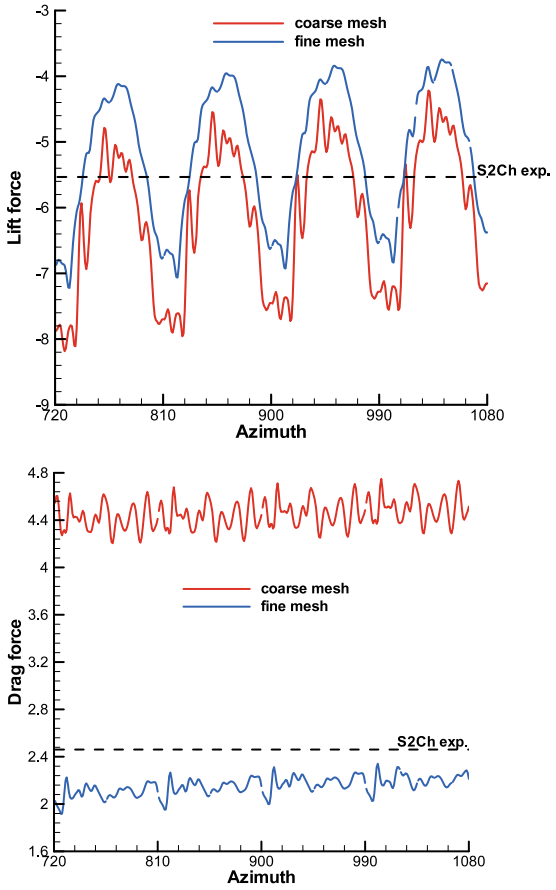

Figure 8 – Effect of the mesh refinement on the fuselage lift and drag histories (ONERA)

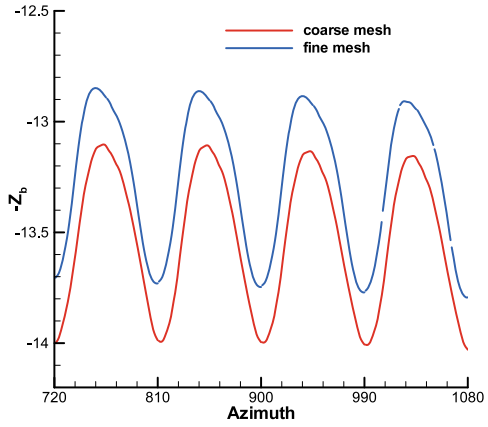

Figure 9 – Effect of the mesh refinement on the rotor thrust evolution (ONERA)

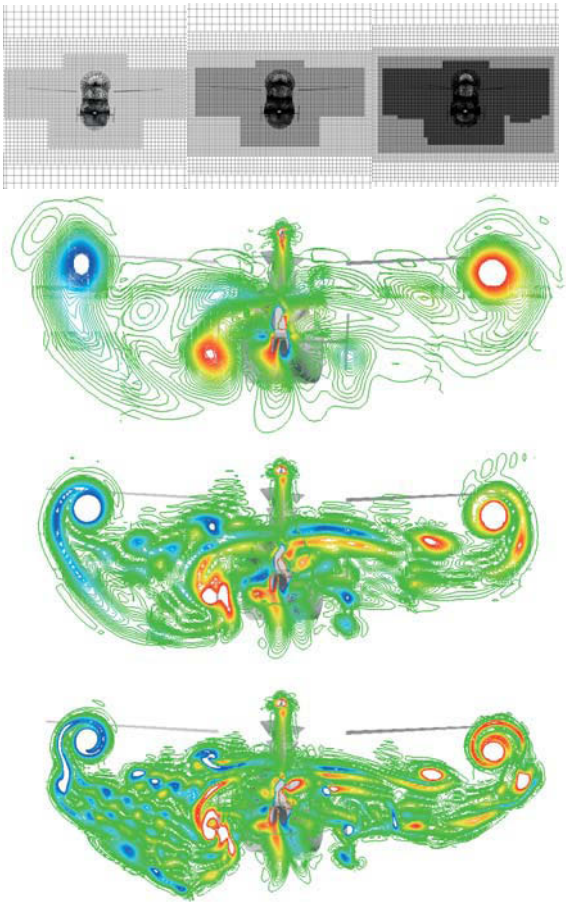

Figure 10 – Effect of mesh refinement on wake capturing, off-body Cartesian mesh spacing 0.40, 0.20, 0.10 * chord (AFDD)

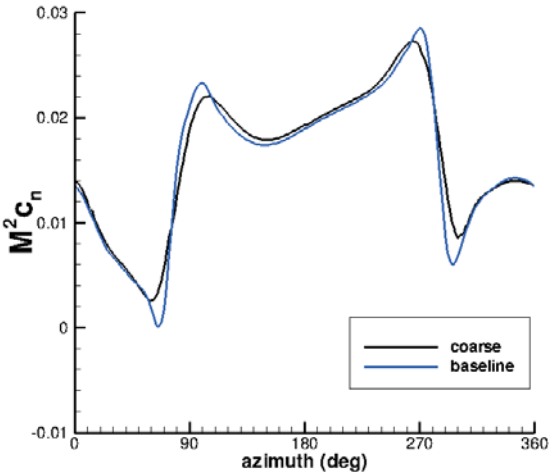

Figure 11 – Effect of mesh refinement on rotor blade airloads, r/R = 0.97 (AFDD)

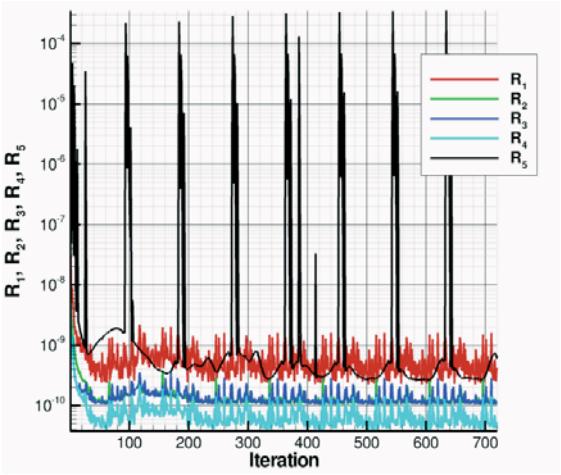

a) coarse grid

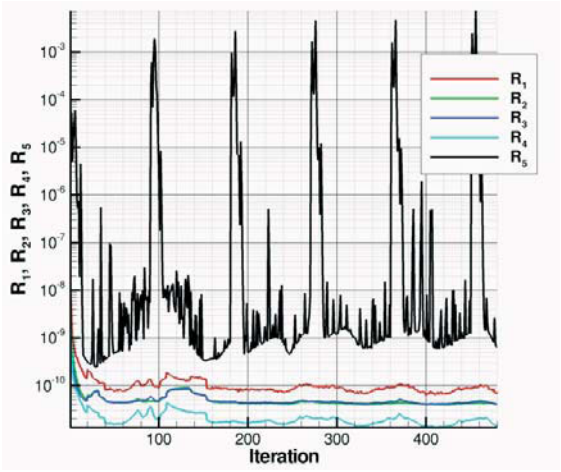

b) fine grid

Figure 12 - Effect of the mesh refinement on the (ρ, u, v, w, turb model) residual histories (GIT)

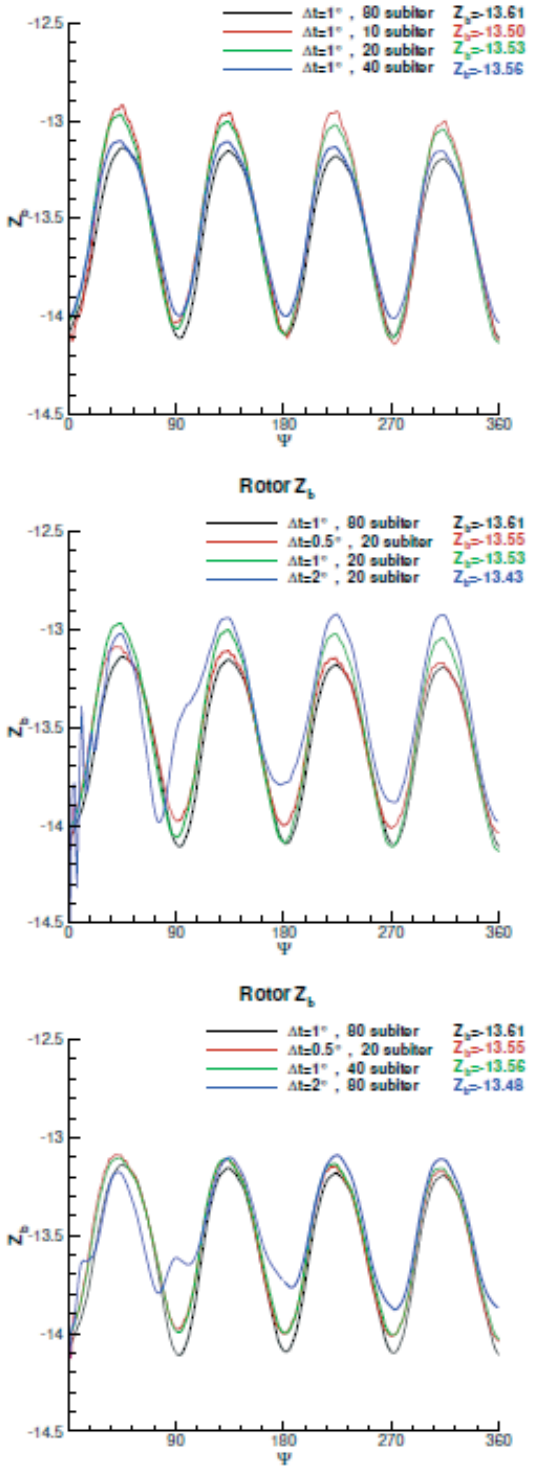

Figure 13 – Temporal convergence history of rotor thrust (ONERA)

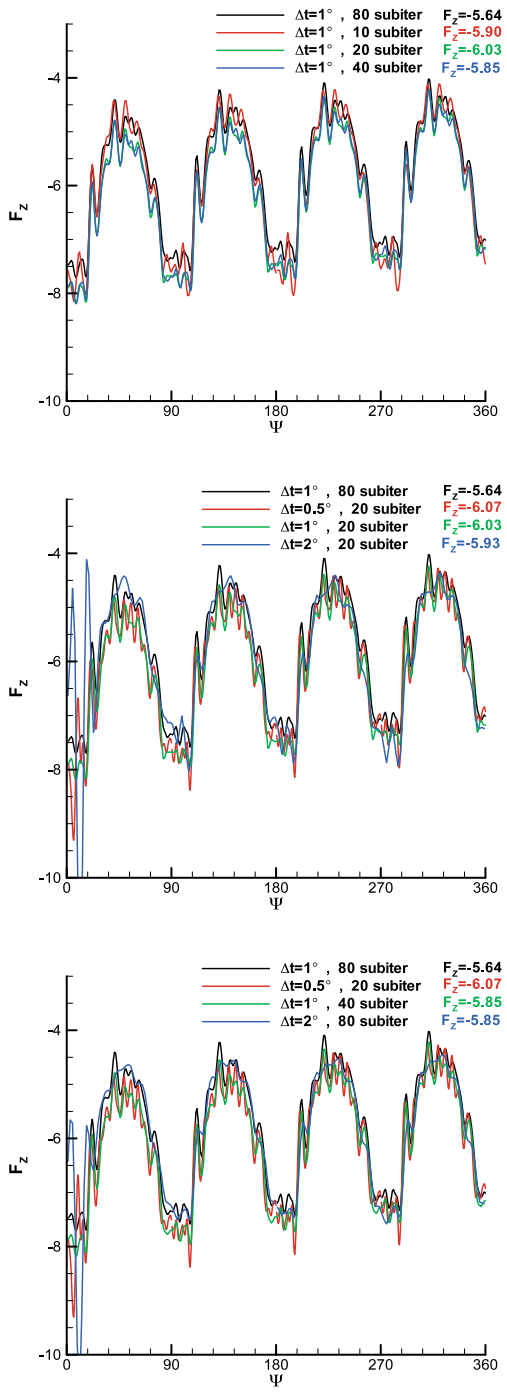

Figure 14 – Temporal convergence history of fuselage lift (ONERA)

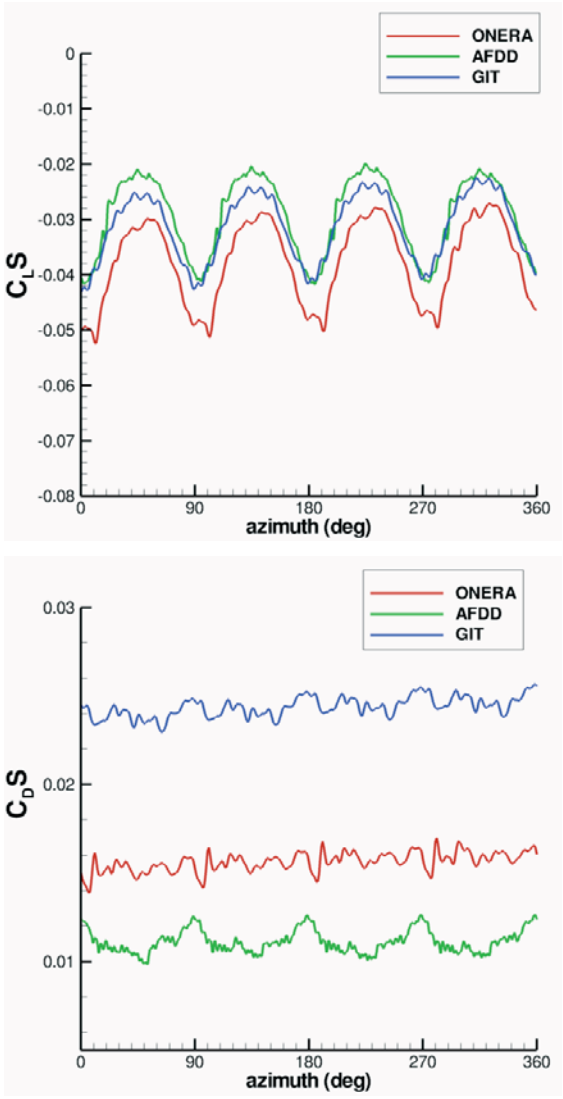

Figure 15 – Fuselage lift and drag time histories

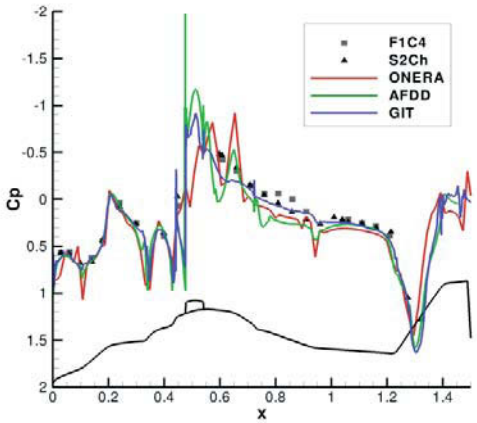

Figure 16 – Fuselage surface pressures, upper centerline, time-averaged

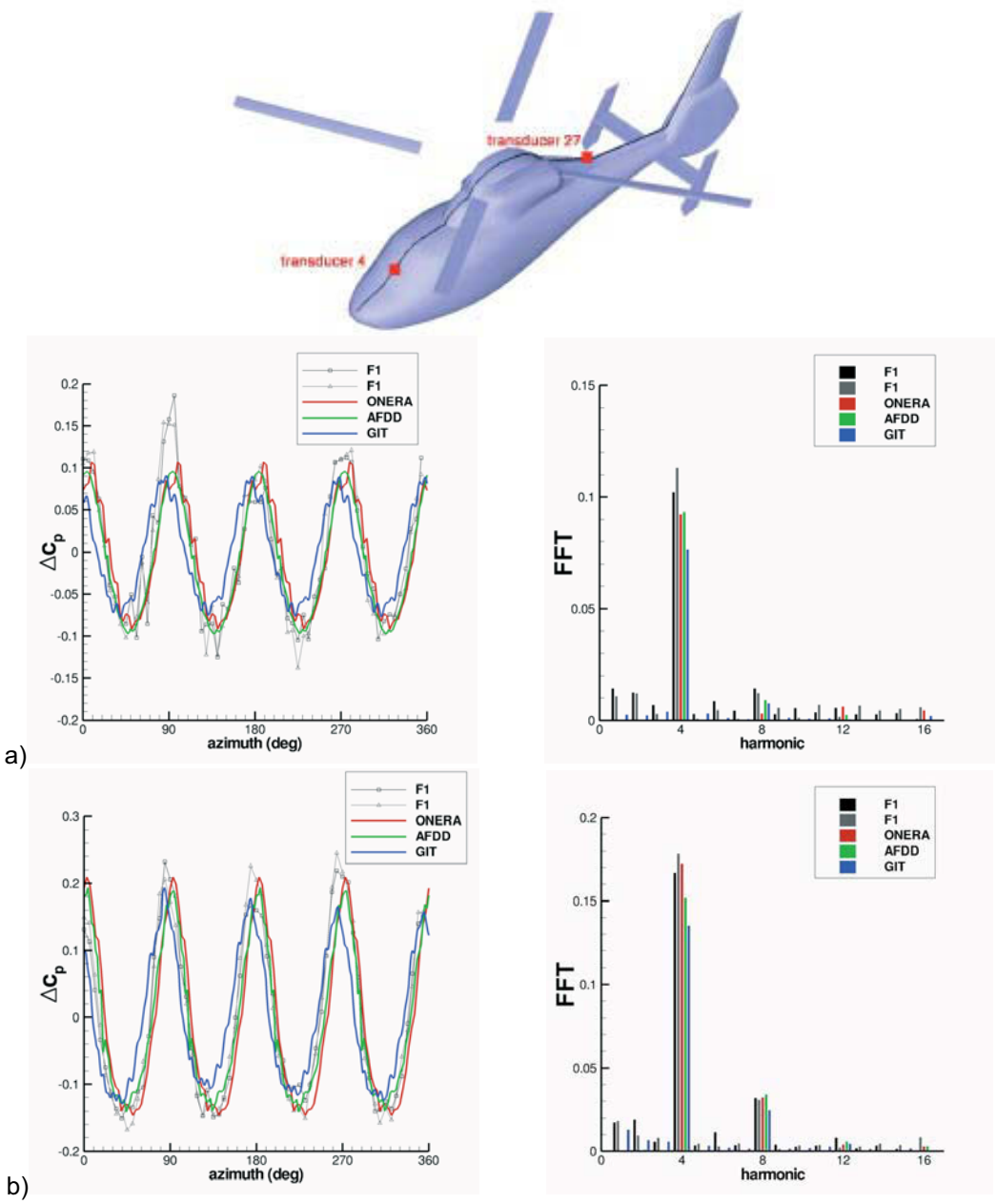

Figure 17 – Unsteady surface pressure time histories and magnitude/frequency, transducer locations a) fuselage nose - 4 and b) tail boom – 27

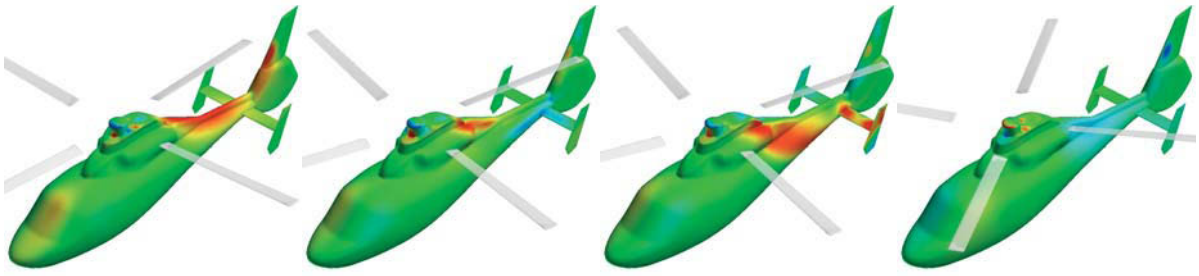

a) AFDD

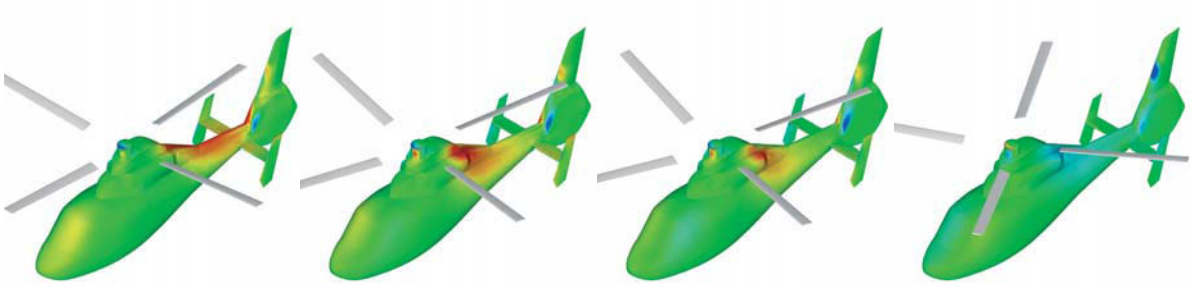

b) GIT

Figure 18 – Unsteady surface pressure differential sequence, ψ = 0°, 14°, 18°, 60°

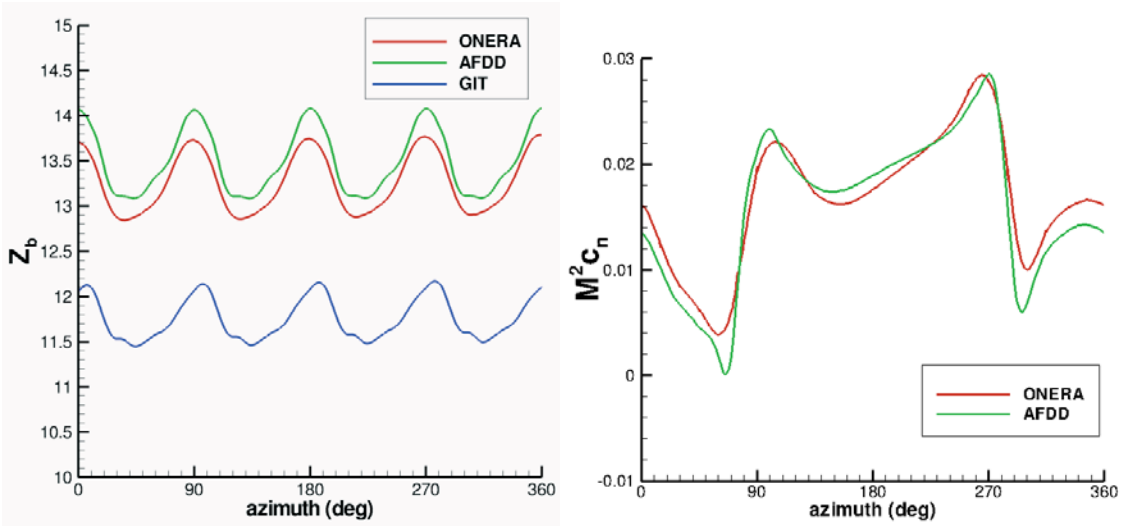

Figure 19 – Rotor thrust (Z_b) and 97% span normal force (M^2c_n) time histories

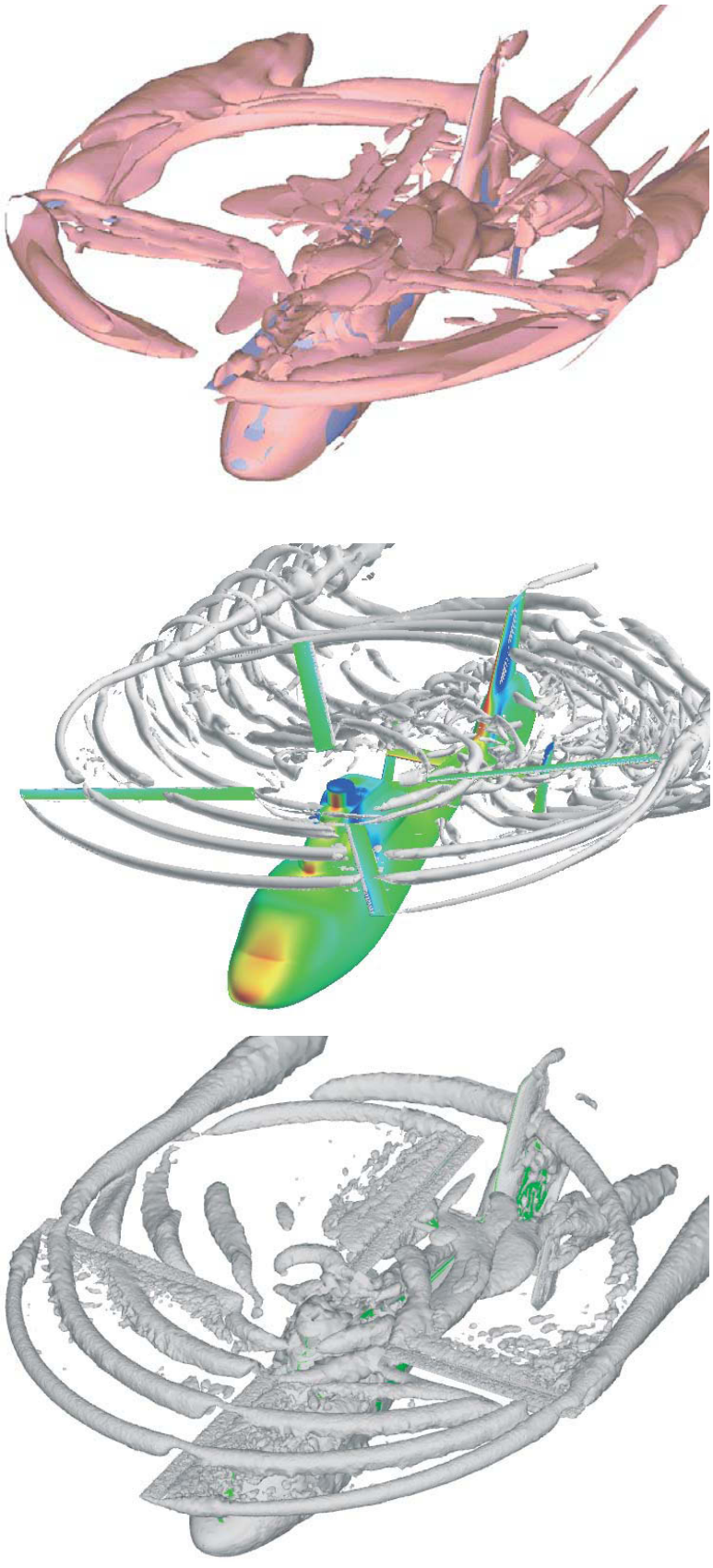

Figure 20 – CFD wake visualization using the Q criterion, a) ONERA, b) AFDD, c) GIT

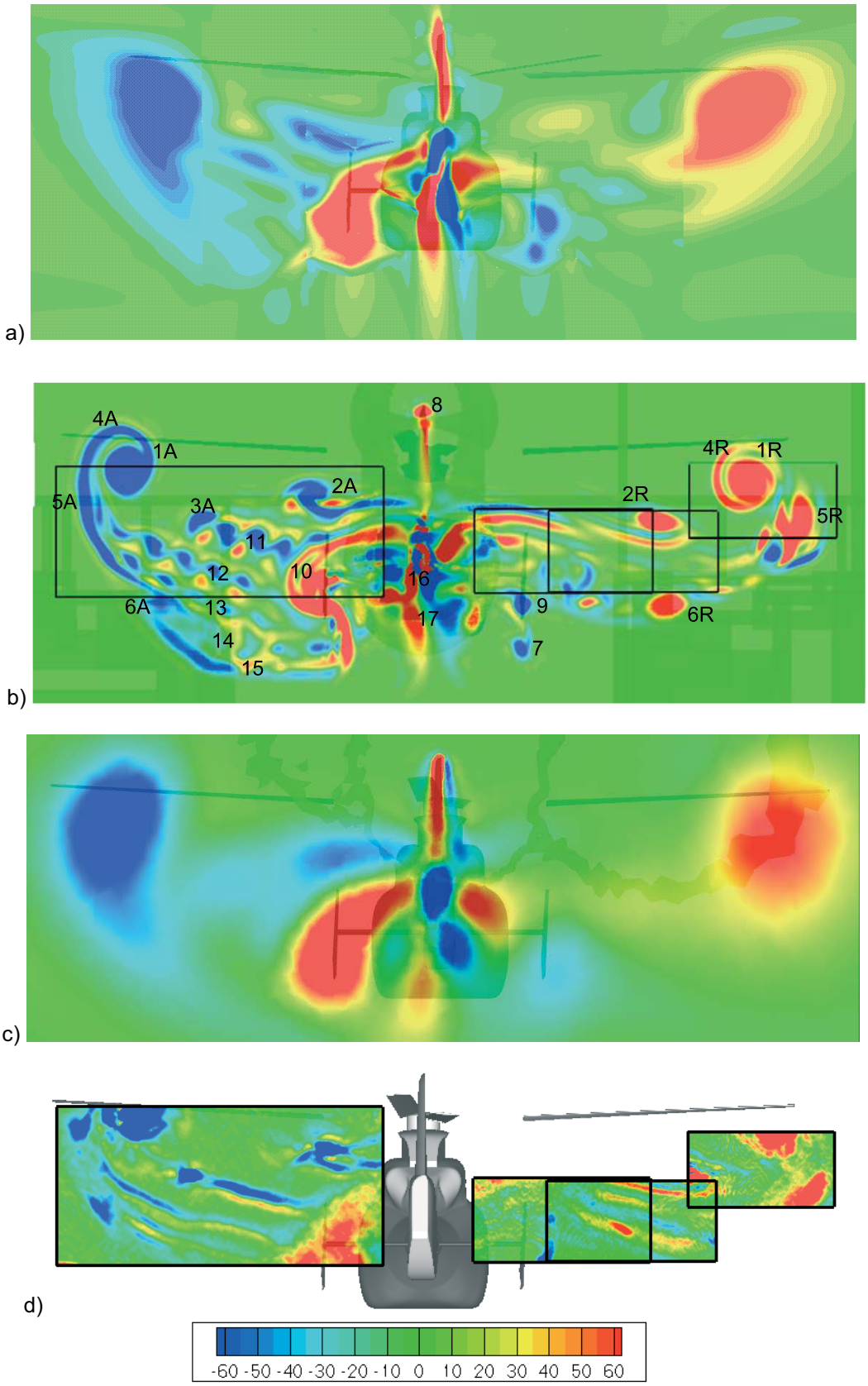

Figure 21 – Comparison of CFD wake flowfield with PIV measurements [Reference 10], plane behind empennage, x-vorticity (sec^{-1}), reference blade at 0 deg azimuth, a) ONERA, b) AFDD, c) GIT, d) 3C PIV

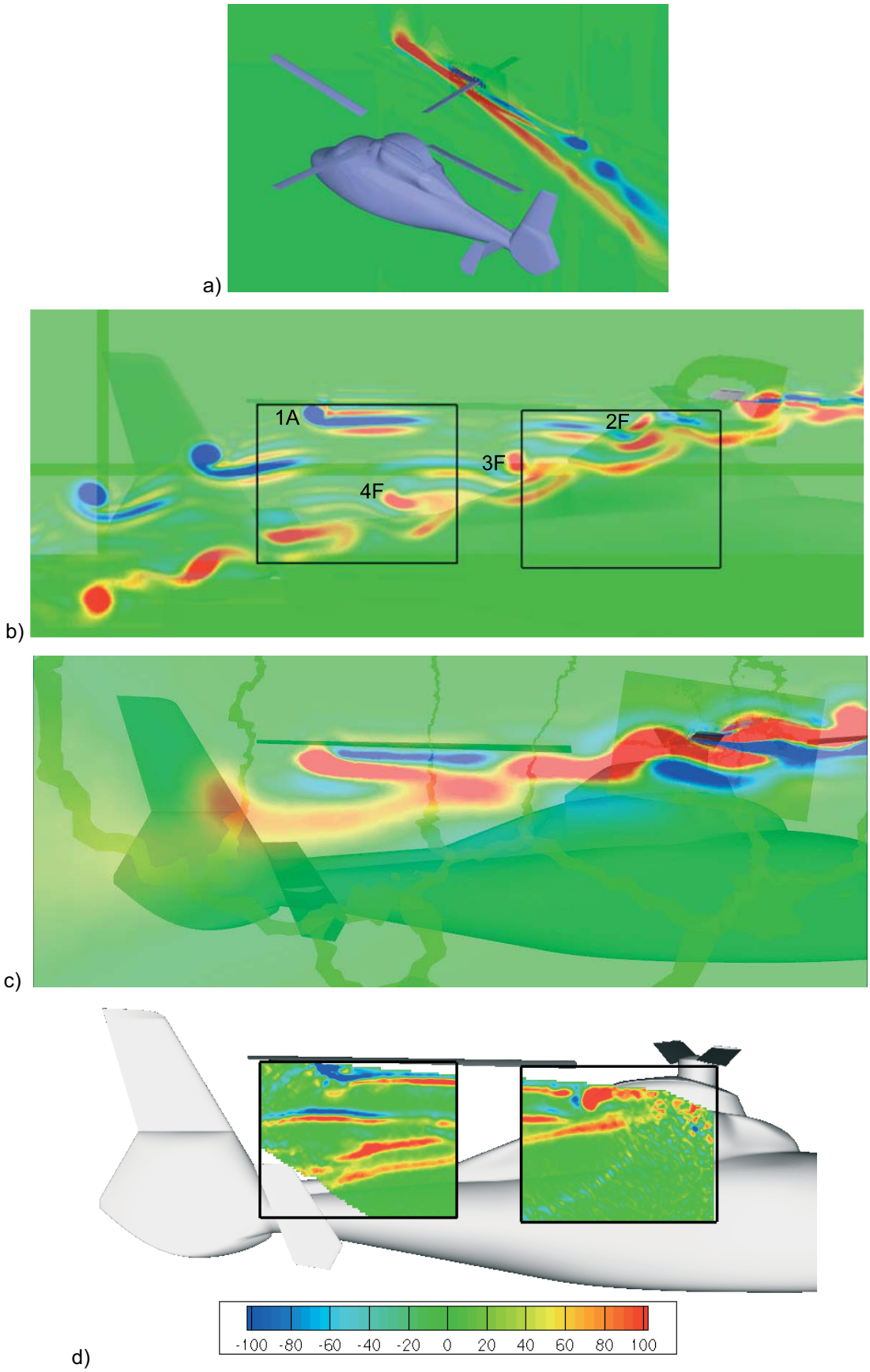

Figure 22 – Comparison of CFD wake flowfield with PIV measurement [Reference 10], retreating side, y-vorticity (sec^{-1}), reference blade at 0 deg azimuth, a) ONERA, b) AFDD, c) GIT, d) 2C PIV